




Combined Effects of Anti-PD-L1 and Nanosonodynamic Therapy on HCC Immune Activation in Mice: An Investigation

Meng Wei^{1,2,*}, Xiaobo Wang^{1,2,*}, Yunhai Mo^{1,2,*}, Cunqing Kong³, Mengqi Zhang^{2,4},
Guanhua Qiu^{2,5}, Zhihong Tang^{1,2}, Jie Chen^{1,2}, Feixiang Wu^{1,2}

¹Hepatobiliary Surgery Department, Guangxi Medical University Cancer Hospital, Nanning, 530021, People's Republic of China; ²Key Laboratory of Early Prevention and Treatment for Regional High Frequency Tumor, Ministry of Education/Guangxi Key Laboratory of Early Prevention and Treatment for Regional High Frequency Tumor, Nanning, 530021, People's Republic of China; ³Medical Imaging Center, Affiliated Taihe Hospital, Hubei University of Medicine, Hubei, 442000, People's Republic of China; ⁴Department of Interventional Therapy, Guangxi Medical University Cancer Hospital, Nanning, 530021, People's Republic of China; ⁵Department of Ultrasound, Guangxi Medical University Cancer Hospital, Nanning, 530021, People's Republic of China

*These authors contributed equally to this work

Correspondence: Jie Chen; Feixiang Wu, Email jiechen185@163.com; wufx2013@163.com

Introduction: Current therapeutic strategies, including immune checkpoint blockade (ICB), exhibit limited efficacy in treating hepatocellular carcinoma (HCC). Nanoparticles, particularly those that can accumulate specifically within tumors and be activated by sonodynamic therapy (SDT), can induce immunogenic cell death (ICD); however, ICD alone has not achieved satisfactory therapeutic effectiveness. This study investigates whether combining ICB with ICD induced by nanoparticle-mediated SDT could enhance anti-tumor immunity and inhibit HCC growth.

Methods: We developed an iron-based micelle nanodelivery system encapsulating the Near-Infrared Dye IR-780, which was surface-modified with a cyclic tripeptide composed of arginine-glycine-aspartic acid (cRGD). This led to the synthesis of targeted IR780@FOM-cRGD nanoparticles. These nanoparticles were specifically engineered to kill tumor cells under sonication, activate immunogenic cell death (ICD), and be used in conjunction with immune checkpoint blockade (ICB) for the treatment of hepatocellular carcinoma (HCC).

Results: The synthesized IR780@FOM-cRGD nanoparticles had an average diameter of 28.23 ± 1.750 nm and a Zeta potential of -23.95 ± 1.926 . Confocal microscopy demonstrated that IR780@FOM-cRGD could target HCC cells while minimizing toxicity to healthy cells. Upon sonodynamic activation, these nanoparticles consumed significant amounts of oxygen and generated substantial reactive oxygen species (ROS), effectively killing tumor cells and inhibiting the proliferation, invasion, and migration of H22 cells. Hemolysis assays confirmed the in vivo safety of the nanoparticles, and in vivo fluorescence imaging revealed significant accumulation in tumor tissues. Mouse model experiments showed that combining ICB (which induced by Anti-PD-L1) with ICD (which induced by IR780@FOM-cRGD), could effectively activate anti-tumor immunity and suppress tumor growth.

Discussion: This study highlights the potential of IR780@FOM-cRGD nanoparticles to facilitate tumor eradication and immune activation when used in conjunction with Anti-PD-L1 therapy. This combination represents a non-invasive, efficient, and targeted approach for the treatment of hepatocellular carcinoma (HCC). By integrating sonodynamic therapy with immunotherapy, this strategy promises to substantially improve the effectiveness of traditional treatments in combating HCC, offering new avenues for clinical application and therapeutic innovation.

Keywords: nanomaterials, sonodynamic therapy, tumor immunity, PD-L1, immunogenic cell death

Introduction

Primary liver cancer, predominantly hepatocellular carcinoma (HCC), ranks among the most prevalent cancer types worldwide, ranking sixth in terms of incidence and third in terms of mortality rates. The global average annual incidence

rate totals 995,000 cases. However, the 5-year average survival rate for HCC remains below 18%.¹ Currently, immunotherapy is emerging as an integral component of multidisciplinary treatment approaches for HCC. Immune checkpoint blockade (ICB) therapies targeting the PD-1/PD-L1 axis have demonstrated significant clinical benefits.²⁻⁴ Nevertheless, the use of PD-1/PD-L1 inhibitors as monotherapy has not resulted in substantial improvements in the clinical prognosis of HCC.^{5,6} In 2021, immune checkpoint blockade (ICB) therapy achieved a noteworthy breakthrough in the management of HCC. The IMbrave150 study revealed that the combination of atezolizumab and bevacizumab extended the overall survival of patients with advanced HCC, representing the first major advancement in frontline treatment for advanced liver cancer in over a decade, since the Sorafenib Hepatocellular Carcinoma Assessment Randomized Protocol and Oriental studies. However, the adverse reactions of this protocol stands at a high rate of 85%, with 49.5% discontinuing treatment due to drug-related adverse events or side effects.⁷ Therefore, there is an urgent need to investigate more effective therapeutic strategies for HCC patients.

Immunogenic cell death (ICD) currently stands as a focal point in tumor research and represents a novel treatment direction. Notably, dying tumor cells have the potential to release tumor-associated antigens (TAA).⁸ Antigen-presenting cells, particularly dendritic cells (DCs), have the capability to capture these antigens and migrate to lymph nodes, where they activate and expand CD4+ and CD8+ T cells. CD8+ cytotoxic T cells can subsequently directly target and eliminate tumor cells. This process constitutes a pivotal aspect of the host-specific immune response.⁹

Sonodynamic therapy (SDT), an emerging therapeutic modality, demonstrates significant potential in inducing immunogenic cell death (ICD) and triggering antitumor immune responses. Leveraging its noninvasive nature and deep tissue-penetrating capabilities, SDT employs sonosensitizers to generate highly cytotoxic reactive oxygen species (ROS), resulting in tumor cell death and the initiation of ICD.¹⁰ Multiple studies by Park et al, Yuan et al, and Zhang et al have indicated that SDT-induced ICD can alter the tumor microenvironment from “cold“ to “hot” and exert inhibitory effects on tumor growth.¹¹⁻¹³ However, some studies suggest that ICD alone may not consistently yield optimal therapeutic outcomes as anticipated.^{14,15} These findings prompt us to consider the distinct mechanisms of action between ICD and ICB in activating the immune system. It thus inspires us to wonder whether their synergistic effects can activate the immune system at different levels, thereby achieving greater anti-tumor therapeutic efficacy, symbolizing the concept of “1+1>2” in tumor treatment. Moreover, SDT for HCC represents an ideal treatment option for several reasons. Firstly, HCC lesions are highly vascularized, with approximately 75% of blood supply derived from arteries, ensuring a continuous oxygen source for SDT.¹⁶ Secondly, given that the liver is a solid organ, ultrasound energy can effectively penetrate and reach tumor locations throughout the liver. Thirdly, SDT is a noninvasive treatment modality, promoting favorable treatment compliance among patients. Lastly, the cost of SDT is relatively low, which not only reduces the financial burden of treatment but also alleviates economic strain on patients. Despite the numerous advantages of Sonodynamic Therapy (SDT), its application is constrained due to the sonosensitizers involved, which are characterized by low water solubility, rapid clearance from the blood, and insufficient accumulation at tumor sites. Recently, there has been a rapid expansion in the application of nanomaterial technology to SDT. Encapsulating sonosensitizers within nanomaterials effectively addresses these drawbacks.¹⁷

Nanomaterials encompass both organic and inorganic categories. Organic nanomaterials are favored for industrial and biomedical applications due to their unique properties such as high porosity, adjustable pore size, and facile functionalization, however, their complex synthesis process, high manufacturing cost, low stability, and long-term safety concerns pose challenges.¹⁸ In contrast, inorganic nanomaterials offer broader application prospects, featuring advantages such as low environmental impact, low cytotoxicity, tunable surface functionalities, and stability under ambient conditions.¹⁹ It is crucial that safety and efficacy are key requirements for the clinical application of medical technologies. Iron oxide nanoparticles are currently the only inorganic nanomaterial approved for clinical use, known for their excellent safety profile.²⁰ Moreover, Nanoparticles of magnetic iron oxide have received much attention due to their biodegradability, low toxicity, and excellent magnetic properties.²¹ Therefore, this study has selected iron oxide nanoparticles as the experimental subject.

Numerous studies have explored the use of nanomaterials in HCC treatment.²² For instance, Wang et al synthesized mesoporous silica nanoparticles conjugated with platinum prodrugs, with lactose acid selected as a liver-targeted ligand for HCC therapy.²³ However, HCC often exhibits resistance to chemotherapy. Bao et al investigated the effects of polyethylene

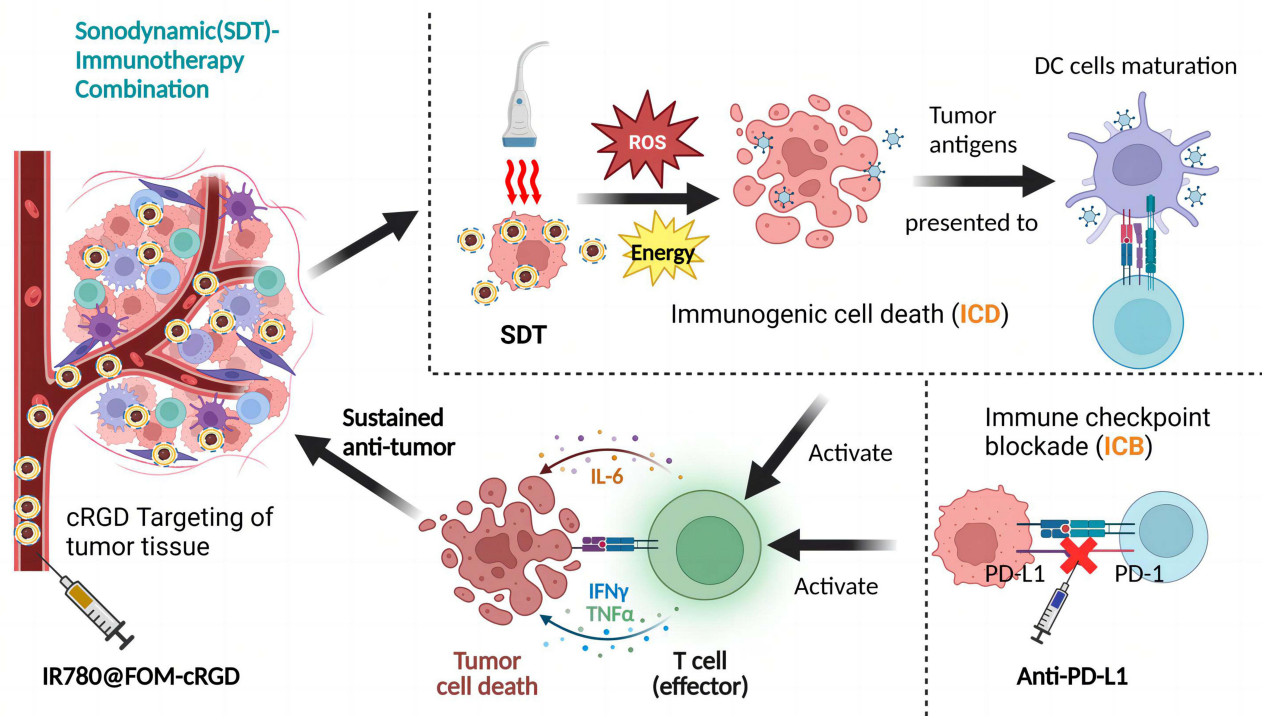


Figure 1 Potential mechanisms of anti-tumor immunity activation by Anti-PD-L1 combined with nanosonodynamic therapy.

glycol (PEG)-modified, platinum-doped carbon nanoparticles (PEG-PtCNPs) on cancer cell viability and migration. Under laser irradiation, these nanoparticles disrupted the tumor cell cytoskeleton, inhibiting metastasis and tumor growth.²⁴ Nonetheless, due to the liver's internal location, light-based treatments encounter challenges in reaching the tumor site.

This study aimed to develop a novel type of IR780@FOM-cRGD nanoparticles (FOM), featuring an Fe_3O_4 core and surface modification with the targeting ligand cyclic arginine-glycine-aspartic acid (cRGD). Cyclic RGD peptides have been extensively utilized as targeting ligands for various anticancer drugs and nanocarriers. In the context of hepatocellular carcinoma (HCC), integrin $\alpha\beta_3$ is known to be overexpressed in carcinoma tissue, and cRGD peptides exhibit specific and strong binding affinity to integrin $\alpha\beta_3$.^{25,26} Studies have shown that the HCC cell line HepG2 exhibits high expression of $\alpha\beta_3$ and enhanced targeting ability of cRGD drugs.²⁷ Additionally, research has demonstrated the high specificity of cRGD to H22 tumors in mice.²⁸ Therefore, we chose the cRGD peptide for its greater stability and selectivity over linear RGD to target H22 cells, facilitating enhanced nanoparticle accumulation in tumor tissue. Encapsulation with FOM within the nanoparticles not only improves the water solubility and optical stability of IR780 iodide in water but also significantly reduces its toxicity to mice. Under sonodynamic therapy (SDT) activation, tumor immunogenic cell death (ICD) can generate neoantigens, activating dendritic cells (DCs) and subsequently T-cells. When combined with immune checkpoint blockade (ICB) therapy, there is further enhancement of therapeutic efficacy against H22 cells and tumors. We hypothesize that such antitumor mechanisms may lead to effective long-term antitumor immunity (Figure 1). In this study, we investigate this hypothesis through *in vitro* and *in vivo* experiments, exploring the effect of SDT treatment based on IR780@FOM-cRGD nanoparticles in combination with anti-PD-L1 therapy on immune modulation in mouse tumor models.

Materials and Methods

The Main Reagents and Animals

Iron(II, III) oxide(Fe_3O_4 , Cat No. I104313-500g, Purity>97%), Oleic Acid (OA, Cat No.112-80-1, Purity>98%), 1-[3-(Dimethylamino)propyl]-3-ethylcarbodiimide hydrochloride(EDC, Cat No.25952-53-8, Purity≥99.0%),

Dimercaptosuccinic acid (DMSA, Cat No. D107254, Purity \geq 98.0%) and N-Hydroxysuccinimide (NHS, Cat No. 6066–82–6, Purity \geq 99.0%) were purchased from Aladdin, Shanghai, China. Dithiothreitol (DTT, Cat No. ab141390, Purity $>$ 99%) was obtained from Abcam, Cambridge, United Kingdom. 1,2-distearoyl-sn-glycero-3-phosphoethanolamine-N-[(polyethylene glycol)-2000]-carboxylic acid (DSPE-PEG2000-COOH, Cat No. F07004, Purity \geq 98.0%) was obtained from Shanghai A.V.T. Pharmaceutical Ltd, China.

2-(N-morpholino) ethanesulfonic acid buffer (MES, Cat No. 4432–31-9, Purity \geq 99%) was purchased from Sigma Aldrich, St. Louis, Missouri. IR780 (Cat No. 4432–31-9, Purity \geq 98%) was purchased from Sigma Aldrich, St. Louis, Missouri. Hoechst 33,342 staining solution and HE staining kit were purchased from SolarBio Technology Co. Ltd. The CCK8 assay kit, TUNEL staining kit, CD3 epsilon rabbit monoclonal antibody, CD8 α rabbit monoclonal antibody, Calreticulin rabbit monoclonal antibody, and Calcium Green-AM/PI for detection were purchased from Beyotime Biotechnology Co. Ltd. The DCFH-DA assay kit was purchased from Funglyn Biotech Inc. Anti-PD-L1 antibody was purchased from Bio X Cell. The IL-6, IL-12, TNF- α , IFN- γ , TGF- β , and IL-10 Elisa assay kits were purchased from Guangzhou Bioscience Co. Ltd. Methanol was purchased from China National Pharmaceutical Group Corporation Chemical Reagent Co. Ltd.

BALB/c female mice aged 6–8 weeks with a bodyweight of 17 ± 2 g were provided by Guangzhou Yancheng Biotech Co., Ltd (Guangzhou, China), and maintained at Guangxi Medical University (Guangxi Experimental Animal Center). All animal experiments were approved by the Ethics Committee for Animal Welfare of Guangxi Medical University, and were conducted in compliance with the China National Standard GB/T35892-2018 Guidelines for Ethical Review of Laboratory Animal Welfare.

Preparation of IR780@FOM-cRGD

Firstly, Fe₃O₄ micelles were synthesized via the thermal decomposition method, with coatings of oleic acid (OA) and dimercaptosuccinic acid (DMSA). Specifically, OA (98% purity, containing 15 mg of iron) and DSPE-PEG2000-COOH (100 mg) were combined and transferred into a 25 mL round-bottom flask containing 10 mL of chloroform. Subsequently, 5 mL of deionized water was gradually added. The mixture was then heated to 65°C and gently stirred for 20 minutes to ensure complete evaporation of the chloroform. This process yielded water-soluble Fe₃O₄-OA-DMSA micelles (FOM) incorporating polyethylene glycol (PEG).

To the previously synthesized PEG-containing FOM, a coupling reaction was initiated by adding 100 mg of 1-ethyl-3-(3-dimethylaminopropyl) carbodiimide hydrochloride (EDC), 90 mg of N-hydroxysuccinimide (NHS), and 20 mL of 2-(N-morpholino)ethanesulfonic acid (MES) buffer (0.02 mol/L, pH 5.5). This mixture was incubated with stirring at room temperature for 20 minutes. Following incubation, the mixture was centrifuged at 100,000g and washed twice with deionized water, then resuspended in 0.02 mol/L borate buffer (pH 8). Subsequently, 10 mg of cyclic arginine-glycine-aspartic acid (cRGD) peptide was gradually added to the suspension, which was continuously stirred for 24 hours at room temperature. The resultant FOM@cRGD conjugate was purified through three washes with deionized water and the removal of excess empty liposomes via ultracentrifugation at 100,000g. Finally, to eliminate large aggregates, the purified FOM@cRGD was subjected to centrifugation at 3000g, resulting in the formation of the target FOM@cRGD.

Finally, IR780, a tricyanocyanine dye, was loaded onto the synthesized PEG-FOM and FOM@cRGD. Specifically, 1 mL of a 1 mg/mL aqueous IR780 solution was added to each formulation and the mixtures were left to shake overnight at room temperature. Unbound IR780 molecules were subsequently removed by ultracentrifugation at 100,000g, resulting in the formation of the desired IR780@FOM and IR780@FOM-cRGD nanoparticles for experimental use.

Characterization of IR780@FOM-cRGD

The morphology and dispersibility of the IR780@FOM-cRGD nanoparticles were characterized using a JEOL-2100F transmission electron microscope (TEM). Additionally, the hydrodynamic size and zeta potential of the nanoparticles were quantitatively determined using a Zetasizer Nano ZS90 dynamic light scattering (DLS) instrument from Malvern, UK.

Nanoparticle Stability Experiment

To evaluate the stability of R780@FOM and IR780@FOM-cRGD nanoparticles, samples of each were incubated in phosphate-buffered saline (PBS) supplemented with 10% serum for 7 days. Dynamic light scattering (DLS) was employed at various time intervals to monitor the dispersion status and size variations of the nanoparticles. This experiment aimed to assess the stability profiles of R780@FOM and IR780@FOM-cRGD under physiological conditions.

In vitro Release Experiment of IR780@FOM-cRGD

IR780@FOM-cRGD nanoparticles were suspended in 10 mL of phosphate-buffered saline (PBS) and subjected to continuous agitation at 60 rpm and 37°C. Supernatants were collected at predetermined intervals (0.5, 1, 2, 4, 6, 8, 10, 12, 24, and 48 hours), immediately replaced with an equivalent volume of fresh PBS. The absorbance of each supernatant was measured using a UV spectrophotometer to determine the concentration of IR780 based on a pre-established standard curve. The cumulative release profile of IR780 from the IR780@FOM-cRGD nanoparticles was then plotted using the obtained data.

Nanoparticle Drug Loading Rate Determination

The concentration of IR780 in the IR780@FOM-cRGD nanoparticles can be quantitatively determined using a UV-Vis spectrophotometer. Given the limited solubility of IR780 in water, a standard solution is prepared by dissolving 2 mg of IR780 in 50 mg of acetonitrile (ACN). An appropriate volume of the nanoparticle sample is then diluted with distilled water to achieve a comparable dilution factor. The IR780 content within the nanoparticles is assessed by comparing the maximum absorbance at approximately 780 nm with that of the standard solution. The loading efficiency of IR780 is subsequently calculated using the formula: IR780 loading (%) = (content of IR780 in nanoparticles / total mass of nanoparticles) × 100%.

Detection of the Cellular Uptake Ability of IR780@FOM-cRGD

The H22 cell line (CL0108) was acquired from Shengen Biotechnology Co., Ltd. (Catalog: SNL-157). Cells (2×10^5) were seeded in a confocal laser-specific culture dish (Diameter/size: 35mm/15mm, Catalog No. 801,002, Nestle Biotechnology Co., Ltd., Wuxi, China) and incubated under standard conditions (37°C, 5% CO₂, 95% humidity) until the cell density reached 50–60%. The original medium was then replaced with 1 mL of fresh culture medium, to which 10 μL of IR780@FOM (1 mg/mL) and IR780@FOM-cRGD (1 mg/mL) were added and incubated for 0.5h and 1h, respectively. Subsequently, the supernatant was removed, and the cells were washed twice with phosphate-buffered saline (PBS). Afterwards, 10 μg/mL of Hoechst 33,342 staining solution was added to each dish. After staining for 5 minutes, cells were washed three times with PBS for 5 minutes each in the dark. The cellular uptake of IR780@FOM and IR780@FOM-cRGD by H22 cells was then visualized using a confocal laser scanning microscope (CLSM) equipped with an excitation wavelength of 750 nm and an emission wavelength of 817 nm (Leica TCS SP8, Germany).

In vitro /vivo Biosafety Evaluation of IR780@FOM-cRGD

In vitro Biosafety Evaluation of IR780@FOM-cRGD

Mouse fibroblast cells (L-929) and alpha mouse liver 12 (AML-12) cells, procured from the Cell Bank of the Shanghai Institute of Biochemistry and Cell Biology, Chinese Academy of Sciences, were seeded in a 96-well plate at a density of 5×10^3 cells/well. After overnight incubation in a CO₂ incubator, the old medium was replaced with fresh medium containing varying concentrations of IR780@FOM-cRGD (1 μg/mL, 5 μg/mL, 10 μg/mL, 20 μg/mL, 50 μg/mL, and 100 μg/mL). After 24 hours, the medium was removed, and 100 μL of 10% CCK8 medium was added to each well. The plates were incubated for 2 hours in the dark, and cell viability was subsequently assessed using a CCK8 assay kit. Optical density (OD) at 450 nm was measured with an ELISA reader (DR6000, Hach Company, Colorado, USA). Cell viability was calculated using the formula: $(OD_{\text{Sample}} - OD_{\text{Blank}}) / (OD_{\text{Control}} - OD_{\text{Blank}}) \times 100\%$. This method quantitatively evaluated the cytotoxicity of the nanoparticles by reflecting cell viability.

In vivo Biosafety Evaluation of IR780@FOM-cRGD

Mice were anesthetized with 1.25% tribromoethanol (Cat No. AB001-M2910, Nanjing Aibei Biotechnology Co., Ltd., dosage: 0.3 mL/20g). A sterile capillary tube was then gently placed against the retro-orbital venous plexus at the corner of the eye socket. The tube was rotated gently and light downward pressure was applied until blood was observed ascending the tube. The required volume of blood was collected promptly. Immediately after collection, gentle pressure was applied to the corner of the eye using a sterile cotton ball to assist in hemostasis. The collected blood was centrifuged at 3000 rpm for 5 minutes to separate the plasma, washed thrice with PBS, and the red blood cells were isolated and resuspended in 8 mL of PBS.

To prepare varying concentrations of IR780@FOM-cRGD solution (0 µg/mL, 1 µg/mL, 5 µg/mL, 10 µg/mL, 20 µg/mL, 50 µg/mL, and 100 µg/mL), 1 mL of the red blood cell suspension was mixed with each concentration. For the positive control, 1 mL of the red blood cell suspension was centrifuged to remove the supernatant, and replaced with 1 mL of deionized water. All samples in EP tubes were gently vortexed and incubated at 37°C for 8 hours, followed by centrifugation to collect the supernatant. Absorbance was measured at 570 nm to assess hemolysis. The hemolysis rate was calculated using the following formula: Hemolysis rate (%) = $(I - I_{\text{PBS}}) / (I_0 - I_{\text{PBS}}) \times 100\%$, where I is the absorbance of different concentrations of IR780@FOM-cRGD nanoparticles against hemoglobin, I_{PBS} is the absorbance of hemoglobin in PBS, and I_0 is the absorbance of complete hemolysis in deionized water.

Evaluation of Toxicity of Nanoparticles for H22 Cells

CCK8 Assay

H22 cells were plated in a 96-well plate and cultured for 24 hours. Subsequently, varying concentrations of IR780@FOM-cRGD (0 µg/mL, 5 µg/mL, 10 µg/mL, 15 µg/mL, 20 µg/mL) were added to the wells, and the cells were exposed to ultrasound therapy using a Shenzhen WED Electronics Medical Co., Ltd. device (Model WED-100). The ultrasound settings were a power density of 1.0 W/cm², a duty cycle of 100%, with the irradiation duration lasting 20 seconds per cycle across nine total cycles, and 30-second intervals between cycles. All treatments were conducted under dark conditions. After an additional 24-hour incubation, the culture medium was removed, and the cells were washed thrice with PBS. Each well was then supplemented with 100 µL of culture medium containing 10% CCK8. After a 2-hour incubation period, cell viability was assessed by measuring the absorbance at 450 nm. The cell proliferation rate was calculated, and the IC₅₀ value for the US+IR780@FOM-cRGD group was determined.

Live/Dead Cell Staining Experiment

H22 cells were prepared as a single cell suspension at a concentration of 1×10^5 /mL and seeded into a 6-well plate, followed by incubation for 24 hours. The cells were then divided into six groups, namely, PBS, US, IR780@FOM, IR780@FOM-cRGD, US+IR780@FOM, and US+IR780@FOM-cRGD, and continued to culture for 2 hours, during which the US, US+IR780@FOM, and US+IR780@FOM-cRGD were subjected to ultrasound treatment (Ultrasound power density was set at 1 W/cm², transducer frequency was set at 1 MHz, and the duration of ultrasound irradiation was 20 seconds with a total of 9 cycles. The interval between two cycles was set at 30 seconds). After an additional 24 hours of incubation and washing with PBS, each well was added with AM/PI detection solution. After incubation for 30 minutes, fluorescence was observed and captured under a fluorescence microscope (Calcein-AM green fluorescence Ex/Em=494/517 nm; PI red fluorescence Ex/Em=535/617 nm).

Flow Cytometry Experiment

H22 cells were seeded in a 6-well plate at a density of 1×10^5 cells/well and incubated for 12 hours. Post-incubation, the cells were divided into six experimental groups: PBS, US (ultrasound), IR780@FOM, IR780@FOM-cRGD, US+IR780@FOM, and US+IR780@FOM-cRGD. The groups designated for ultrasound treatment (US, US+IR780@FOM, and US+IR780@FOM-cRGD) underwent ultrasound exposure under the previously specified conditions. After 2 hours, the cells were harvested, centrifuged, and then resuspended in 100 µL of binding buffer. In a subsequent step conducted under dark conditions, 5 µL of FITC-Annexin V and 5 µL of propidium iodide (PI) were added to each

sample. The mixtures were then incubated at room temperature in the dark for 15 minutes. Following incubation, 400 μL of binding buffer was added to each tube. The apoptotic rate of the cells was subsequently analyzed using a flow cytometer (Model: CALIBUR, BD (Becton, Dickinson and Company), USA, Software Version: FlowJo_v10.8.1).

Colony Formation, Transwell Invasion and Migration Assay

Colony Formation Assay

H22 cells were seeded in a 6-well plate at a density of 5×10^3 cells per well. After 24 hours, the cells were assigned to one of six groups: PBS, US (ultrasound), IR780@FOM, IR780@FOM-cRGD, US+IR780@FOM, and US+IR780@FOM-cRGD. Two hours later, the groups designated for ultrasound treatment were exposed to US irradiation under dark conditions. Prior to the irradiation, the culture medium in each respective well was replaced with fresh medium. The cells were subsequently cultured in a medium containing 10% fetal bovine serum for approximately 14 days, with medium replacements every two days.

After the incubation period, the colonies were fixed with methanol and stained with 0.1% crystal violet. Colony formation was assessed by counting the stained colonies, providing a measure of cell proliferation and survival under the various treatment conditions.

Transwell Invasion Assay

Matrix gel (100 μL) was applied to the upper chamber of a Transwell and allowed to solidify for 30 minutes. H22 cells were then suspended in serum-free medium at a density of 2.5×10^5 cells/mL, and 200 μL of this cell suspension was added to the upper chamber. After 12 hours, the cells were categorized into six groups: PBS, US (ultrasound), IR780@FOM, IR780@FOM-cRGD, US+IR780@FOM, and US+IR780@FOM-cRGD. Two hours later, the groups designated for ultrasound treatment underwent US irradiation under dark conditions using previously specified parameters. Concurrently, a 24-well culture plate containing 750 μL of medium with 10% fetal bovine serum (FBS) was positioned in the lower chamber to serve as a chemoattractant, and the cells were cultured for an additional 48 hours.

Post-incubation, the upper chamber was removed, washed twice with PBS, and the non-migrated cells in the upper chamber were mechanically removed. Cells that had migrated to the lower chamber were fixed with 4% paraformaldehyde for 20 minutes and stained with crystal violet for 15 minutes. Migration was evaluated by capturing images under an optical microscope, providing quantitative and visual evidence of cell migratory behavior under the various treatment conditions.

Transwell Migration Assay

The same procedures as previously described for the Transwell invasion assay were followed, with the exception that matrix gel was not added to the upper chamber. This modification facilitated the assessment of cell migration independently of invasive capabilities, allowing for a direct comparison of cell motility across the different treatment groups.

Detection of in vitro ROS Production

H22 cells were seeded in a 6-well plate at a density of 2×10^5 cells per well and incubated for 24 hours. Subsequently, the cells were allocated into six distinct groups: PBS, US (ultrasound), IR780@FOM, IR780@FOM-cRGD, US+IR780@FOM, and US+IR780@FOM-cRGD, and received corresponding treatments. After treatment, the cells were incubated with 2',7'-dichlorodihydrofluorescein diacetate (DCFH-DA) detection solution for 20 minutes in serum-free medium to assess the intracellular reactive oxygen species (ROS) levels. The ROS levels were then measured using inverted fluorescence microscopy, providing insights into oxidative stress responses induced by the various treatments.

In vivo Fluorescence Imaging of Small Animals

All animal experiments were approved by the Animal Welfare and Ethics Committee of Guangxi Medical University (Ethics number: LW2024064). H22 cell suspension (100 μL , 1×10^6 cells) was injected subcutaneously into the back of

BALB/C mice to construct an H22 tumor-bearing mouse model. When the tumor volume reached 1000 mm³, IR780@FOM and IR780@FOM-cRGD were intravenously injected via the tail vein at 0 hours. Near-infrared imaging was performed at 0 h, 4 h, 8 h, and 12 h to record the changes in fluorescence intensity at different time points in the tumor-bearing mice.

The Role of IR780@FOM-cRGD in Mouse Tumor Development

Female BALB/c mice were subcutaneously injected with 1×10^6 H22 cells into their backs. After 6 days, the mice were randomly divided into four groups: (1) PBS control group; (2) US+IR780@FOM-cRGD group; (3) Anti-PD-L1 group; and (4) US+IR780@FOM-cRGD+Anti-PD-L1 combination therapy group. IR780@FOM-cRGD was administered intravenously via the tail vein at a dosage of 5 mg/kg. Ultrasound irradiation was performed on days 0, 2, and 4 post-injection using a regimen with a power density of 1.0 W/cm² and a duty cycle of 100%. Each ultrasound session consisted of nine cycles, with each cycle lasting 20 seconds and 30-second intervals between cycles. Anti-PD-L1 antibody was administered intravenously via the tail vein at a dose of 75 µg per mouse on days 1, 3, and 5. Throughout the experiment, the mice were monitored for body weight, body temperature, and tumor growth. Tumor volume was assessed and documented every other day. Measurements of tumor size were performed using a Vernier caliper, and tumor volume was calculated using the following formula: tumor volume $V(\text{mm}^3) = (\text{width}^2 \times \text{length})/2$. According to the animal experimental protocol, mice were euthanized when tumor volumes reached 2000 mm³. Tumors were harvested and sectioned into 5 µm slices for histopathological analysis. The production of reactive oxygen species (ROS) within the tumor sections was assessed using the DCFH-DA (2',7'-dichlorofluorescein diacetate) fluorescence probe. DNA damage was detected using the γ-H2AX monoclonal antibody, while the proliferation of tumor cells was evaluated with the Ki-67 monoclonal antibody. Additionally, DNA fragmentation and apoptosis were analyzed using the TUNEL assay, providing a comprehensive assessment of the tumor microenvironment and the efficacy of the therapeutic interventions.

Detection of Immune Activation Markers in Mice

Cytokine Detection

Upon conclusion of the experiment, blood samples were collected from the mice for cytokine analysis. An ELISA kit provided by Guangzhou Bioscience Corporation was utilized to measure serum levels of inflammatory cytokines including IL-6, IL-12, tumor necrosis factor-alpha (TNF-α), and interferon-gamma (IFN-γ), as well as anti-inflammatory cytokines such as transforming growth factor-beta (TGF-β) and IL-10. This assessment was conducted to evaluate the acute inflammatory response following treatment, offering insights into the immunological impacts of the therapeutic interventions.

DC Cell Level Detection

Dissected mouse tumor tissues were cut into small pieces (<2 mm³) and enzymatically dissociated to isolate individual cells. An appropriate volume of trypsin-EDTA solution was added to the tissue, gently mixed, and incubated at 37°C for 30–60 minutes. The trypsinization process was halted using DMEM culture medium supplemented with 10% fetal bovine serum. The resulting cell suspension was then filtered through a 40-micron cell strainer to remove undigested tissue fragments and debris. Subsequently, the cells were centrifuged at 400×g and 4°C, the supernatant discarded, and the pellet resuspended in cold PBS with 2% FBS until the desired concentration was achieved. Cell concentration was adjusted to 1×10^6 cells/mL, and Fc receptor blocking antibodies were added to minimize non-specific binding prior to staining. Cells were incubated with fluorescently-labeled CD80 and CD86 dendritic cell (DC) antibodies at 4°C for 30 minutes. Following incubation, cells were washed three times with PBS to remove excess antibodies, centrifuged, and resuspended in 400 µL of PBS for analysis. Flow cytometry was performed using a CALIBUR flow cytometer (Becton, Dickinson and Company, USA), with data analyzed using FlowJo software (Version 10.8.1). Dendritic cell populations were identified based on forward scatter (FSC) and side scatter (SSC) parameters. Levels of DC cells were quantified for each experimental group and compared to the control group to assess immune response modulation following treatment.

Detection of Immunological-Related Immunohistochemical Markers

Preparation of Tumor Section

Mouse tumor tissues were harvested and fixed in 4% paraformaldehyde (PFA) for 24 hours. Following fixation, tissues underwent dehydration through a series of graded ethanol solutions, were embedded in paraffin blocks, and sectioned at 4–5 μm thickness using a microtome. The sections were then mounted onto glass slides.

Deparaffinization and Antigen Retrieval

Paraffin-embedded sections were deparaffinized in xylene and rehydrated through graded ethanol. Antigen retrieval was conducted by heating the sections in a 10 mM citrate buffer (pH 6.0) in a water bath.

Blocking and Permeabilization

Sections were blocked with 5% bovine serum albumin (BSA) in PBS to prevent non-specific binding and permeabilized with 0.1% Triton X-100 in PBS for cellular membrane disruption.

Immunostaining

Sections were incubated overnight at 4°C with primary antibodies diluted in 1% BSA in PBS. The primary antibodies applied included rabbit anti-CD3epsilon, rabbit anti-CD8 α , CRT monoclonal antibody, and FOXP3 monoclonal antibody. After rinsing with PBS, sections were incubated with fluorescently labeled secondary antibodies at room temperature for one hour.

Mounting and Imaging

Following secondary antibody application, sections were mounted with a mounting medium and covered with slips. Immunofluorescently stained sections were examined under a microscope using appropriate fluorescence filters, and images were captured.

Image Analysis

Quantitative analysis of the immunofluorescent signals was conducted using Image J software. This analysis helped determine the expression levels of immunological markers in the mouse tumor tissues.

Detection of in vivo Biosafety Indicators

Following the completion of the experiment, mice were humanely euthanized via CO₂ inhalation. Key organs such as the heart, liver, spleen, lungs, kidneys, and blood samples were harvested for analysis. Hematoxylin and eosin (H&E) staining was performed on tissue sections for histological examination. Additionally, standard biochemical assays were conducted to assess various biochemical indicators pertinent to liver and kidney functions, as well as overall hematological parameters.

Statistical Analysis Methods

Data were analyzed using descriptive statistics and variance analysis, and results are presented as means \pm standard deviation. Independent sample *t*-tests and analysis of variance (ANOVA) were employed for inter-group comparisons. A *p*-value greater than 0.05 was considered statistically non-significant. All analyses were conducted in triplicate across three independent experiments. Significance levels are denoted as follows: **p*<0.05, ***p*<0.01, ****p*<0.001, *****p*<0.0001.

Results and Discussions

Preparation and Characterization of IR780@FOM-cRGD

In the presence of surfactants, FOM nanoparticles were synthesized by thermally decomposing metal acetylacetonate (Acac) and encapsulating Oleic Acid (OA). Subsequent modifications of the synthesized FOM involved the conjugation of polyethylene glycol (PEG) and cyclic arginine-glycine-aspartic acid (cRGD) peptides, resulting in the formation of IR780@FOM and IR780@FOM-cRGD. These nanoparticles exhibit an ideal magnetic-core lipid-shell structure, as shown in Figure 2A. Electron microscopy imaging revealed that both IR780@FOM and IR780@FOM-cRGD

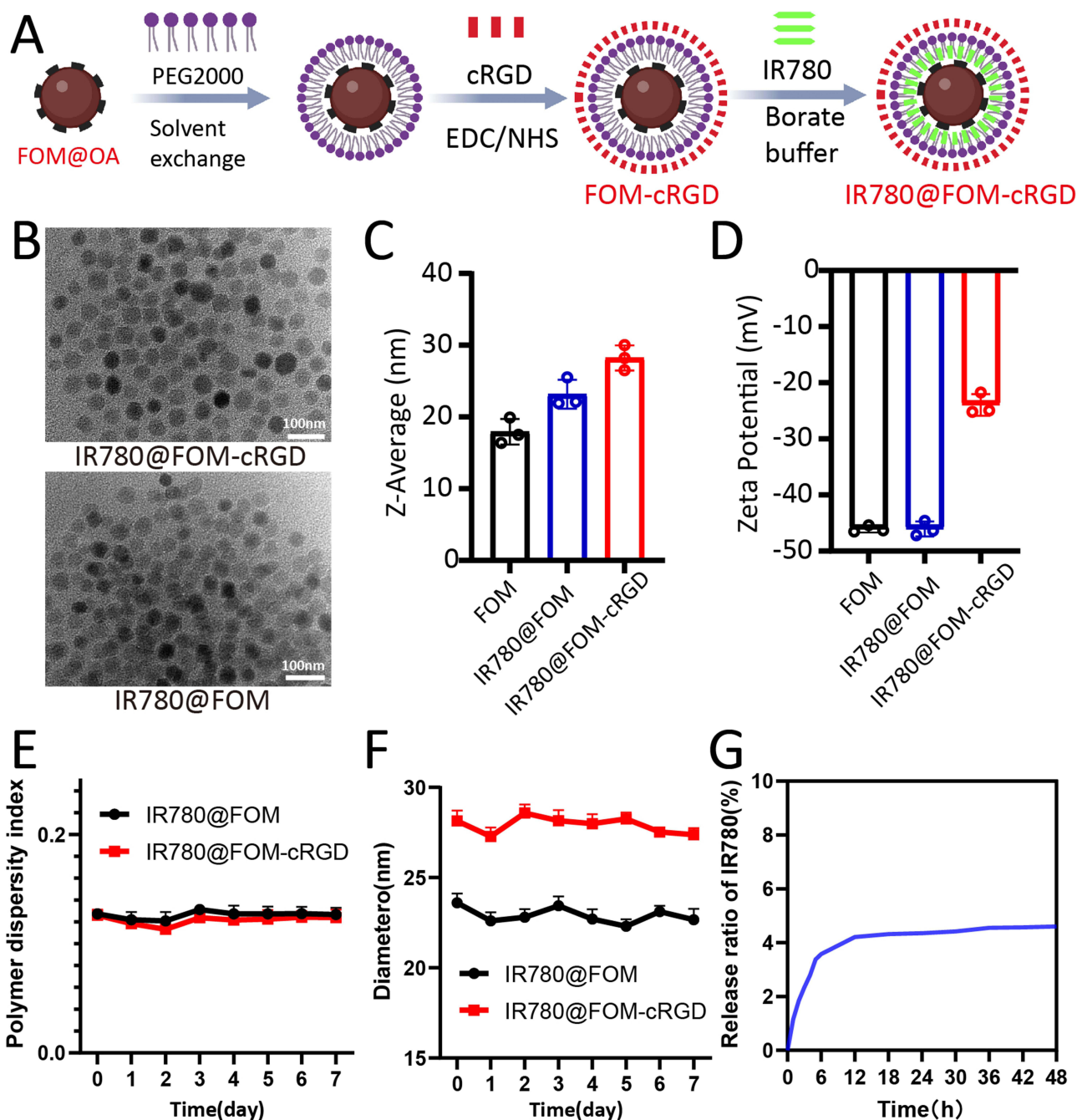


Figure 2 Characterization of IR780@FOM-cRGD. (A) Schematic illustration of the synthetic procedure for IR780@FOM-cRGD nano-materials. (B) Morphological observation of synthesized IR780@FOM and IR780@FOM-cRGD nano-particles under electron microscopy. (C) Dynamic light scattering analysis of nano-particle size for FOM, IR780@FOM, and IR780@FOM-cRGD. (D) Electrophoretic light scattering analysis of Zeta potential for FOM, IR780@FOM, and IR780@FOM-cRGD nano-particles. (E and F) Dispersion status (E) and particle size changes (F) of IR780@FOM and IR780@FOM-cRGD in PBS. (G) In vitro release detection of IR780@FOM-cRGD.

nanoparticles possess a uniform and well-dispersed spherical structure with consistent size distribution (Figure 2B). Dynamic light scattering (DLS) analysis indicated that the diameters of FOM, IR780@FOM, and IR780@FOM-cRGD nanoparticles are 17.93 ± 1.790 nm, 23.17 ± 2.023 nm, and 28.23 ± 1.750 nm, respectively (Figure 2C). The increase in diameters following the loading of IR780 and cRGD suggests successful incorporation of these functional groups. Correspondingly, the Zeta potentials were measured as -46.08 ± 0.5915 , -46 ± 1.317 , and -23.95 ± 1.926 mV, respectively (Figure 2D). Notably, IR780@FOM-cRGD exhibits a Zeta potential within the range of +30 to -30 mV, suggesting

enhanced stability and biocompatibility due to reduced likelihood of aggregation within this range.²⁹ Results from the Nanoparticle Stability Experiment indicated no significant changes in polymer dispersity index (PDI) and particle size for both samples, as demonstrated in Figures 2E and F. This consistency in size and PDI suggests that the nanoparticles exhibited good dispersion and stability over the duration of the experiment.³⁰ This stability provides a strong foundation for the subsequent utilization and storage of these nanoparticles in nanomedicine applications. The *in vitro* release curve of IR780@FOM-cRGD, as depicted in the figure, shows that the cumulative release of IR780 increases over time. However, after 12 hours, the release of IR780 reaches a plateau, stabilizing at a release rate of no more than 5% (Figure 2G). This plateau indicates the excellent stability of IR780@FOM-cRGD, highlighting its potential for sustained delivery applications.

Furthermore, the drug loading rate detection results reveal that the loading rate of IR780 in the nanoparticles was $5.31 \pm 0.28\%$. When compared to the drug loading rates reported in similar studies— $3.46 \pm 0.03\%$ for folate-modified liposomal nanoparticles by Jiao Song et al, and 3.06% for polymeric shells based on poly(propylene glycol-b-polyethylene glycol) by Sijie Chen et al—the FOM nanomicelles synthesized in this study demonstrate a superior drug loading capacity. This higher drug loading rate offers significant advantages, including enhanced drug delivery efficiency and reduced dosage requirements, making these nanoparticles highly advantageous for therapeutic applications.^{31,32} The comprehensive characterization of the aforementioned nanomaterials conclusively demonstrates the successful synthesis of these nanostructures.

The Biocompatibility and Cellular Uptake of IR780@FOM-cRGD

The results of the CCK8 assay revealed that IR780@FOM-cRGD exerted minimal impact on the viability of L-929 and AML-12 healthy cells across a concentration range of 0–100 $\mu\text{g/mL}$. Cell viability remained largely unchanged with increasing concentrations (Figure 3A). This experiment underscores the low cytotoxicity of IR780@FOM-cRGD towards normal cells, demonstrating its favorable *in vitro* safety profile.^{33,34} The hemolysis assay results demonstrated that the hemolysis rate remained below 10% for concentrations of IR780@FOM-cRGD up to 100 $\mu\text{g/mL}$ (Figure 3B). This finding indicates that IR780@FOM-cRGD possesses favorable *in vivo* safety characteristic.³⁵ As the concentration of IR780@FOM-cRGD nanoparticles increased, their cytotoxic efficacy against tumor cells under ultrasound activation also enhanced, achieving an IC₅₀ value of 5.204 $\mu\text{g/mL}$ (Figure 3C). This result demonstrates that IR780@FOM-cRGD exhibits high efficiency in killing and inhibiting tumor cells when activated by ultrasound, identifying 5.204 $\mu\text{g/mL}$ as a critical reference concentration for future cellular experiments.³⁶

Confocal fluorescence imaging results demonstrated that the red fluorescence intensity within the cytoplasm of H22 cells co-cultured with IR780@FOM was relatively weaker at 0.5h and 1h post nanoparticle addition. In contrast, the red fluorescence from IR780@FOM-cRGD was significantly stronger at these time points (Figure 3D). Notably, at 1h post addition, the fluorescence intensity in H22 cells treated with IR780@FOM-cRGD was considerably higher compared to that in pancreatic cancer (Pan02) and colorectal cancer cells (MC38), highlighting the enhanced targeting capability of IR780@FOM-cRGD specifically towards H22 cells. These observations align with findings by Biyuan Zheng et al, who reported high target specificity towards H22 tumor cells using silicon phthalocyanine nanoparticles decorated with cRGD ligands.²⁸ These findings collectively suggest that both IR780@FOM and IR780@FOM-cRGD nanoparticles are capable of being internalized into the cytoplasm of various tumor cells. However, the cRGD-modified IR780@FOM-cRGD demonstrates enhanced targeting capabilities specifically towards H22 cells. This ensures a sufficient accumulation of the nanomedicine within H22 cells, potentially enhancing therapeutic efficacy.³⁷

The *in vitro* Cytotoxic and Inhibitory Effects of IR780@FOM-cRGD

After culturing, H22 cells were divided into six treatment groups: PBS, US, IR780@FOM, IR780@FOM-cRGD, IR780@FOM+US, and IR780@FOM-cRGD+US. A series of assays, including flow cytometry-assisted apoptosis analysis (Figure 4A), live-dead cell staining (Figure 4B and S1A), Transwell migration (Figure 4C), Transwell invasion (Figure 4D), and colony formation assays (Figure 4E), were conducted. The results indicated that cytotoxicity and inhibitory effects on proliferation, invasion, and migration of H22 cells were less pronounced in the control and single

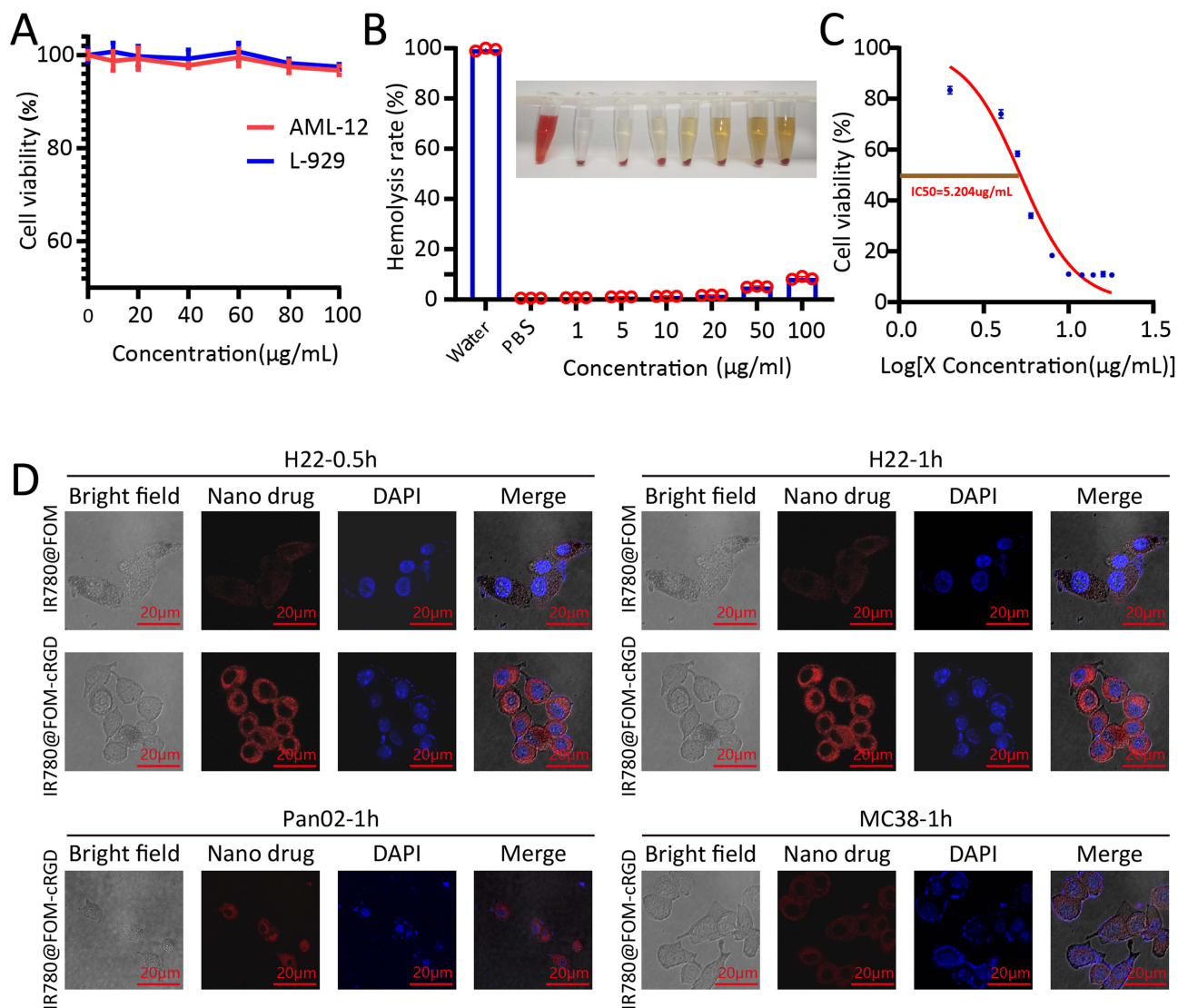


Figure 3 The biocompatibility and cellular uptake of IR780@FOM-cRGD. **(A)** The CCK8 assay assessed the toxicity of increasing concentrations of IR780@FOM-cRGD on AML-12 and L-929 cells. **(B)** Hemolysis rates of red blood cells were analyzed with an ELISA reader after adding IR780@FOM-cRGD nanoparticles at different concentrations to deionized water and PBS with centrifuged red blood cells. **(C)** The IC₅₀ of IR780@FOM-cRGD under ultrasound stimulation was determined using the CCK8 assay. **(D)** The uptake ability of H22, Pan02 and MC38 cells for IR780@FOM-cRGD nanoparticles was evaluated after adding nanoparticles, respectively, using confocal microscopy.

treatment groups (PBS, US, IR780@FOM, IR780@FOM-cRGD) compared to the combination therapy groups. Notably, the IR780@FOM-cRGD+US group exhibited the most significant therapeutic efficacy.

These findings suggest that once internalized by tumor cells in substantial quantities, IR780@FOM-cRGD can significantly enhance the apoptosis of these cells and inhibit their invasive, migratory, and proliferative capacities when activated by ultrasound. This underscores the potential of IR780@FOM-cRGD as a powerful agent for targeted ultrasound-mediated therapy.³⁸ IR780 is a well-known sonosensitizer. Previous research has demonstrated that ultrasound can induce mechanical vibrations of sonosensitizer molecules, generating significant thermal effects and ROS. These effects can cause structural damage to cells and induce apoptosis in tumor cells. This mechanistic insight highlights the therapeutic potential of IR780 in ultrasound-mediated cancer treatments, where its properties are harnessed to enhance cell cytotoxicity and apoptotic responses.^{32,39} The results presented in Figure 4A corroborate this mechanism; under ultrasound activation, the IR780@FOM and IR780@FOM-cRGD groups exhibit significantly increased mechanical damage compared to the PBS, US, IR780@FOM, and IR780@FOM-cRGD groups, particularly in the first quadrant.

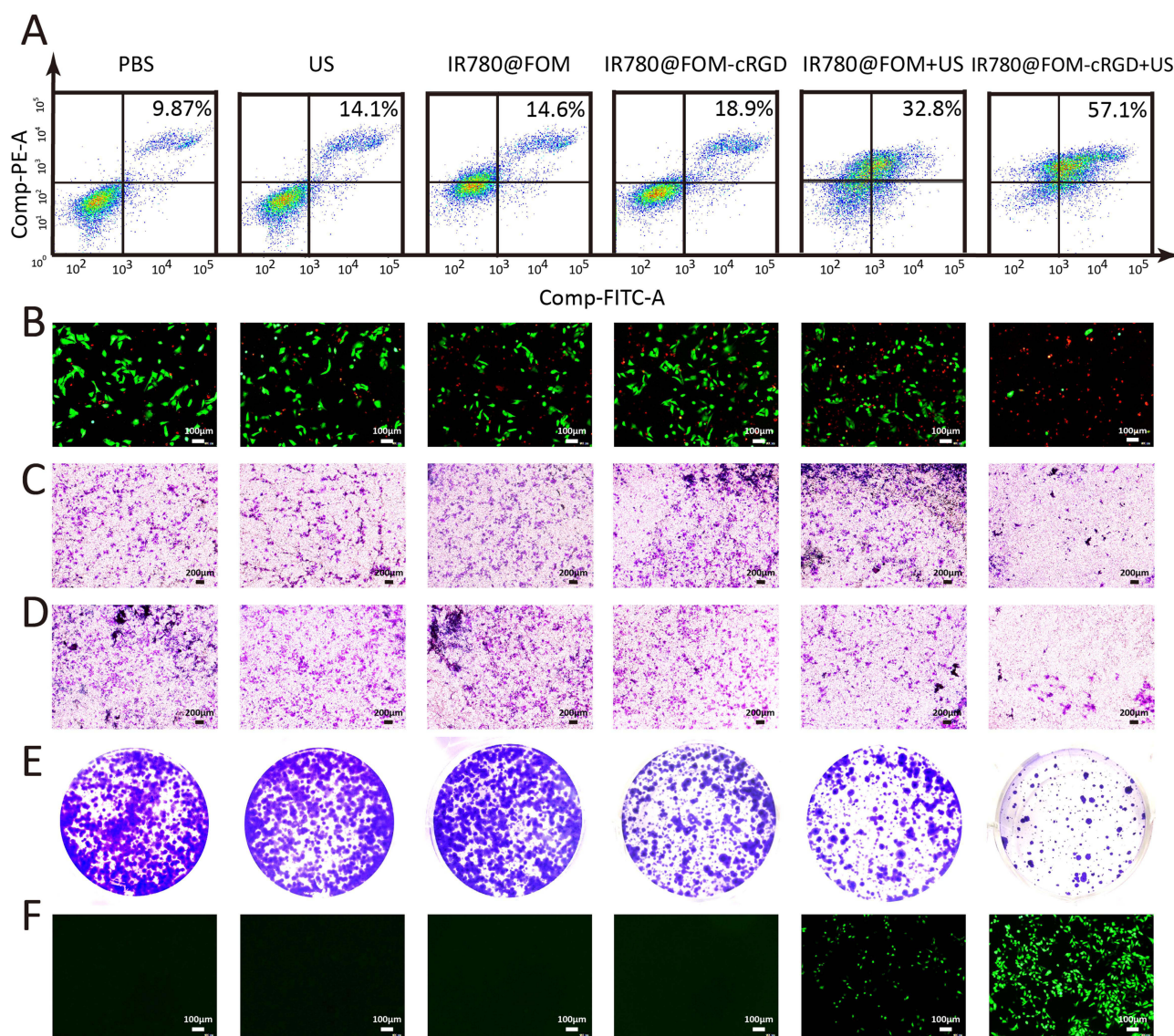


Figure 4 The in vitro cytotoxic and inhibitory effects of IR780@FOM-cRGD. (A and B) Flow cytometry (A) and live-dead staining (B) were used to evaluate the cytotoxic effects of PBS, US, IR780@FOM, IR780@FOM-cRGD, US+IR780@FOM, and US+IR780@FOM-cRGD on H22 cells. (C-D) Transwell migration (C) and invasion assays (D) were employed to assess the inhibitory effects of the six treatment groups on the invasion and migration capacity of H22 cells. (E) A colony formation assay was employed to evaluate the proliferation of H22 cells across six treatment groups. (F) Additionally, ROS detection reagents were utilized to assess the impact of the six treatments on ROS production.

Furthermore, upon ultrasound activation, sonosensitizers like IR780 can generate reactive oxygen species (ROS). These ROS contribute to cellular oxidative stress and lipid peroxidation, which in turn damages cell membranes and organelles, ultimately leading to tumor cell death. This elucidates the dual mechanism of ultrasound-mediated therapy, leveraging both mechanical and oxidative stress to enhance antitumor efficacy.⁴⁰ Similar to the study conducted by An Jie et al, who synthesized a mitochondria-targeting nano platform CDP@HP-T with surface-loaded photosensitizer CE6, this nano platform, when activated by ultrasound, generates abundant reactive oxygen species (ROS), exerting potent cytotoxic effects on tumor cells, resulting in complete tumor eradication and suppression of tumor recurrence in mice.⁴¹

The results of ROS detection in this study further confirm that under ultrasound activation, the production of ROS is significantly increased in both the IR780@FOM and IR780@FOM-cRGD groups. Notably, due to the targeted delivery facilitated by cRGD, ROS production is highest in the IR780@FOM-cRGD group (Figure 4F and S1B). These findings indicate that upon rapid internalization by H22 cells, IR780@FOM-cRGD, in conjunction with ultrasound and its

sonosensitizing properties, can generate substantial amounts of ROS. This leads to both mechanical and ROS-induced cellular damage in H22 cells, highlighting the dual therapeutic mechanisms of this nano platform.

Fluorescence Imaging Analysis of IR780@FOM-cRGD

IR780 is not only a photosensitizer but also a near-infrared fluorescent dye, which has the ability to perform near-infrared imaging.⁴² Its maximum excitation wavelength is around 700–900 nm, which enables it to penetrate through the deeper regions of biological tissues.⁴³ Therefore, it has been widely applied in the field of biomedical imaging technology, particularly in near-infrared fluorescence imaging.³¹ Results from small animal fluorescence imaging demonstrated strong fluorescence signals at the tumor site post tail vein injection of nanoparticles in both groups. Notably, the fluorescence intensity in the IR780@FOM-cRGD group was significantly stronger than that in the IR780@FOM group at 0, 4, 8, and 12 hours post-injection (Figure 5A and B). These observations suggest that IR780@FOM-cRGD possesses enhanced tumor-targeting capabilities, making it a promising candidate for tumor imaging. As such, IR780@FOM-cRGD could potentially be utilized for non-invasive imaging to ascertain the location, size, and morphology of tumors, providing crucial information for diagnostic and therapeutic applications.⁴⁴ Organ fluorescence imaging in mice revealed distinct patterns of nanoparticle distribution: IR780@FOM primarily accumulated in the lungs, whereas IR780@FOM-cRGD showed relatively low accumulation in the heart, liver, spleen, lungs, and kidneys (Figure 5C). This distribution pattern indicates that IR780@FOM-cRGD exhibits a high degree of tumor-targeting specificity and minimal accumulation in normal tissues. These findings underscore the enhanced safety profile of IR780@FOM-cRGD, reflecting its potential as a targeted therapeutic agent with reduced risk of systemic toxicity.⁴⁵

Anti-PD-L1 Combined with Nanoscale Sonodynamic Therapy on Mouse Tumor

This study demonstrates that IR780@FOM-cRGD possesses targeted tumor capabilities and, when activated by ultrasound, the sonosensitizer generates a significant amount of reactive oxygen species (ROS) within the tumor, leading to tumor cell destruction. The resultant cellular damage and lysis release various tumor antigens, including heat shock proteins, ATP, and DNA. These antigens are captured by antigen-presenting cells, predominantly dendritic cells (DCs), which in turn promote their maturation. Mature DCs then present these antigens to T cells, initiating an adaptive immune response. This process leads to persistent immune-mediated eradication of tumor cells, a mechanism known as immunogenic cell death (ICD). This highlights not only the therapeutic efficacy of IR780@FOM-cRGD in direct

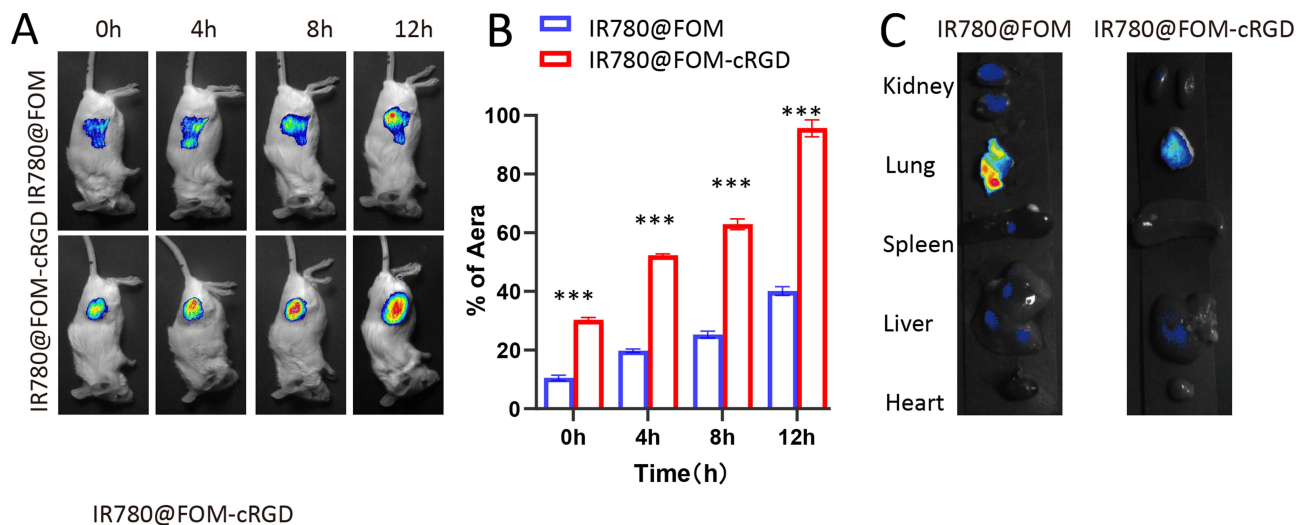


Figure 5 Fluorescence imaging analysis of IR780@FOM-cRGD. (A) Representative images of small animal fluorescence imaging at 0h, 4h, 8h, and 12h after intravenous injection of IR780@FOM and IR780@FOM-cRGD in BALB/C mice at 0h. (B) Quantitative comparative analysis of fluorescence in mouse tumors. (C) Organ fluorescence imaging of mice's heart, liver, spleen, lungs, and kidneys after sacrifice. Statistical analysis was conducted using a two-tailed non-paired t-test, where significance levels were denoted as follows: ***For $P < 0.001$.

tumor ablation but also its potential to enhance antitumor immunity.⁴⁶ However, the capacity of immunogenic cell death (ICD) alone to activate the human immune system and effectively inhibit or kill tumor cells is limited. Tumor cells often employ immune escape mechanisms that allow them to evade immune surveillance. Among the most significant of these mechanisms is the PD1/PD-L1 immune checkpoint pathway. This pathway plays a critical role in dampening the immune response, enabling tumor cells to persist and proliferate despite the immune system's efforts to eliminate them.⁴⁶⁻⁴⁹ PD-L1, by binding with its receptor PD-1, inhibits the immune activity of activated T cells, B cells, and natural killer cells, thus avoiding being attacked and eliminated by the immune system.⁵⁰ Anti-PD-L1 antibodies can bind to PD-L1 and block the process of tumor cell escape.⁵¹ Currently, PD-L1 immune checkpoint blockade therapy (ICB) has achieved good results in the combination treatment of liver cancer, but its side effects are also significant. Moreover, the therapeutic effect of PD-L1 monotherapy is still unsatisfactory.⁵² Therefore, this study aims to combine the ICD effect produced by sonodynamic therapy with ICB treatment to fully activate the tumor immune response, thereby inhibiting tumor growth while minimizing side effects.

In this study, tumor-bearing mice were allocated into four treatment groups: PBS control, IR780@FOM-cRGD+US, Anti-PD-L1, and IR780@FOM-cRGD+US+Anti-PD-L1. Our findings revealed no significant differences in body weight and temperature among these groups post-treatment (Figure 6A and B). Notably, the IR780@FOM-cRGD+US+Anti-PD-L1 group demonstrated the most substantial inhibitory effect on tumor growth compared to the other groups (Figure 6C). Immunohistochemical analysis indicated significantly elevated ROS levels in the tumor tissues of both the IR780@FOM-cRGD+US and IR780@FOM-cRGD+US+Anti-PD-L1 groups (Figure 6D and SI1B), confirming that ultrasound stimulation of IR780@FOM-cRGD effectively promotes ROS generation. Furthermore, the IR780@FOM-cRGD+US+Anti-PD-L1 group exhibited increased levels of the DNA damage-related protein γ -H2AX (Figure 6E and SI1C) and a significant rise in the apoptotic protein TUNEL (Figure 6F and SI1D), while the proliferation-related protein Ki-67 was markedly reduced (Figure 6G and SI1E). These results suggest that the synergistic treatment involving Anti-PD-L1 and IR780@FOM-cRGD under ultrasound stimulation provides a more potent tumor-suppressive effect than either Anti-PD-L1 or IR780@FOM-cRGD+US treatment alone. This combination strategy enhances tumor cell apoptosis, DNA damage, and reduces cellular proliferation, thereby amplifying anti-tumor efficacy.

Anti-PD-L1 Combined with Nanoscale Sonodynamic Therapy Promotes Antitumor Immune Activation

The results demonstrate that the combination therapy of IR780@FOM-cRGD+US+Anti-PD-L1 significantly inhibits tumor growth and induces cytotoxicity in mouse tumors. In addition to the direct cytotoxic effects mediated by ultrasound-activated sonosensitizers, this study also raises the question of whether the mouse immune system has been effectively activated as a result of the treatment. Previous studies have established that activation of the tumor immune response can lead to alterations in various cytokine levels, suggesting a systemic immunological engagement. Understanding whether such activation occurs in response to this combination therapy could provide deeper insights into its mechanisms of action and potential for inducing a durable immune-mediated antitumor response.⁵³ In this study, serum levels of representative cytokines were measured to assess immune system activation. The results indicated that, compared to the IR780@FOM-cRGD+US and Anti-PD-L1 groups, the combination therapy of IR780@FOM-cRGD+US+Anti-PD-L1 significantly elevated the levels of pro-inflammatory cytokines IL-6, TNF- α , and IFN- γ , while concurrently reducing the production of anti-inflammatory cytokines IL-10 and TGF- β (Figure 7A). This cytokine profile suggests an enhanced immunogenic response, potentially facilitated by immunogenic cell death (ICD). ICD is known to activate dendritic cells (DCs), promoting their maturation and differentiation. This enhances their antigen-presenting and immune-regulatory capabilities, thereby amplifying the immune system's capacity to target and eliminate tumor cells. This mechanism underscores the potential of combining ICD-inducing therapies with immune checkpoint inhibitors to robustly stimulate anti-tumor immune responses.⁵⁴ Therefore, this study measured the level of mature DC cells in tumor tissues. Results of flow cytometric analysis showed that the levels of mature DC cells in the IR780@FOM-cRGD+US+Anti-PD-L1 group were significantly higher than those in other groups (Figure 7B). Similar to the research conducted by Zecong Xiao et al, they utilized mannose as a targeting ligand for modification, delivering de-methylating enzyme inhibitor-loaded nanoparticles carrying tumor-

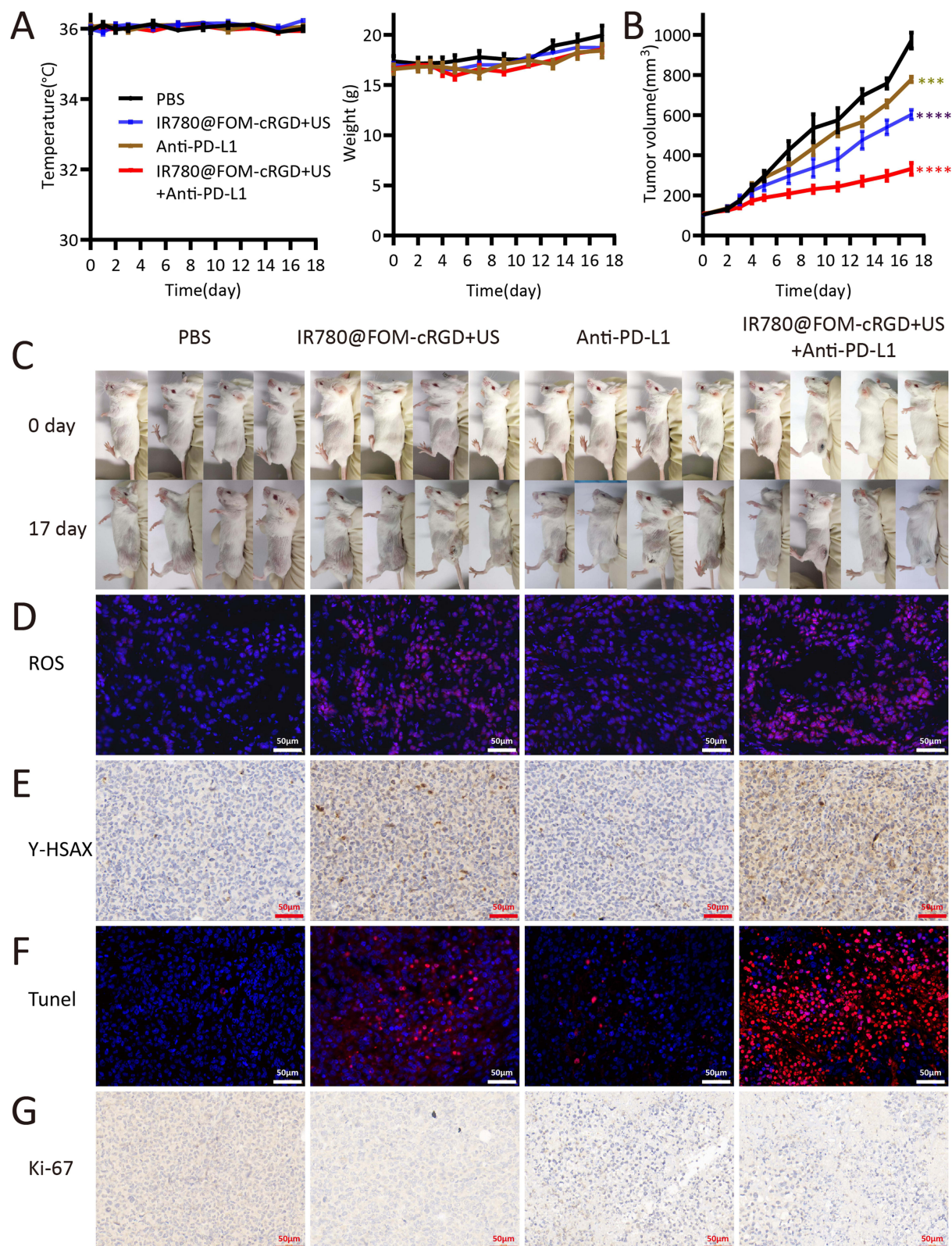


Figure 6 Effect of Anti-PD-L1 combined with Nano-sonodynamic Therapy on tumor in mice. (**A–C**) BALB/C mice were subcutaneously injected with H22 cells to establish a mouse tumor model. The mice were divided into four groups: PBS group, US+IR780@FOM-cRGD group, Anti-PD-L1 group, and US+IR780@FOM-cRGD+Anti-PD-L1 group. The body temperature and weight (**A**) of the mice were measured every other day, and the size of the tumors (**B**) was recorded by taking representative images (**C**) of the tumors after 7 days. (**D–G**) Immunohistochemistry was used to stain ROS (**D**), γ -HSAX (**E**), TUNEL (**F**), and Ki67 (**G**) in mice tumor tissues to determine the level of ROS production, DNA damage level, apoptosis and proliferation level within the tumors. Statistical analysis was conducted using a two-tailed non-paired *t*-test, where significance levels were denoted as follows: ***for $P < 0.001$, and ****for $P < 0.0001$.

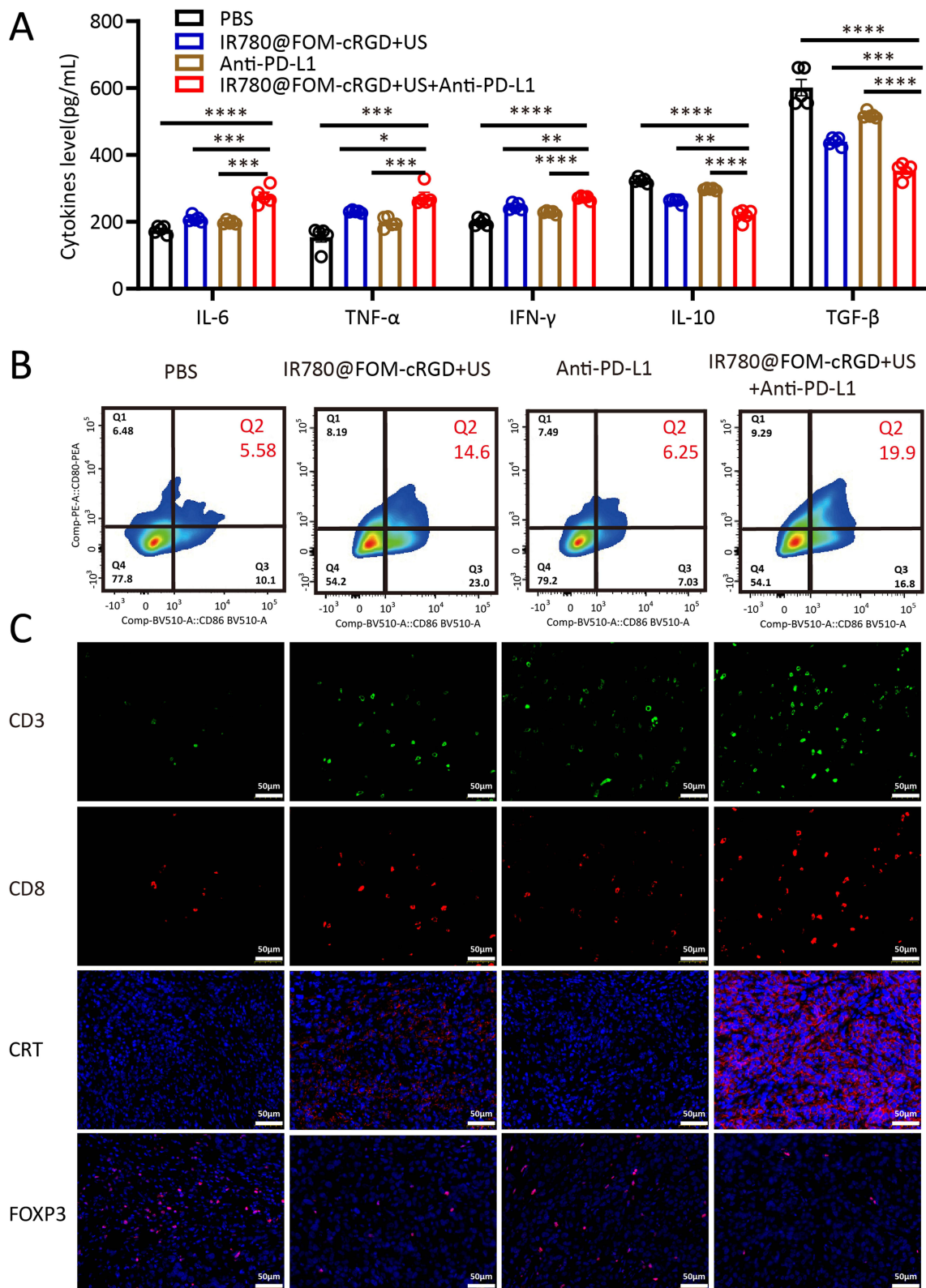


Figure 7 Effect of Anti-PD-L1 combined with Nano-sonodynamic Therapy on tumor immunity in mice. **(A)** On day 18 post-tumor inoculation, the serum of mice in the PBS group, IR780@FOM-cRGD+US group, Anti-PD-L1 group, and IR780@FOM-cRGD+US+Anti-PD-L1 group was collected to measure the levels of IL-6, TNF- α , IFN- γ , IL-10, and TGF- β . **(B)** The tumor from each group of mice was harvested to prepare single-cell suspensions. Flow cytometry analysis with CD80 and CD86 antibodies was performed to assess the level of mature DC cells in each treatment group. **(C)** The tumor tissue from each group of mice was stained with CD3, CD8, CRT, and FXP3 antibodies using immunohistochemical staining to evaluate the infiltration of CD3+ and CD8+ T cells, the status of immunogenic cell death, and immunosuppression. Statistical analysis was conducted using a two-tailed non-paired *t*-test, where significance levels were denoted as follows: *for $P < 0.05$, **for $P < 0.01$, ***for $P < 0.001$, and ****for $P < 0.0001$.

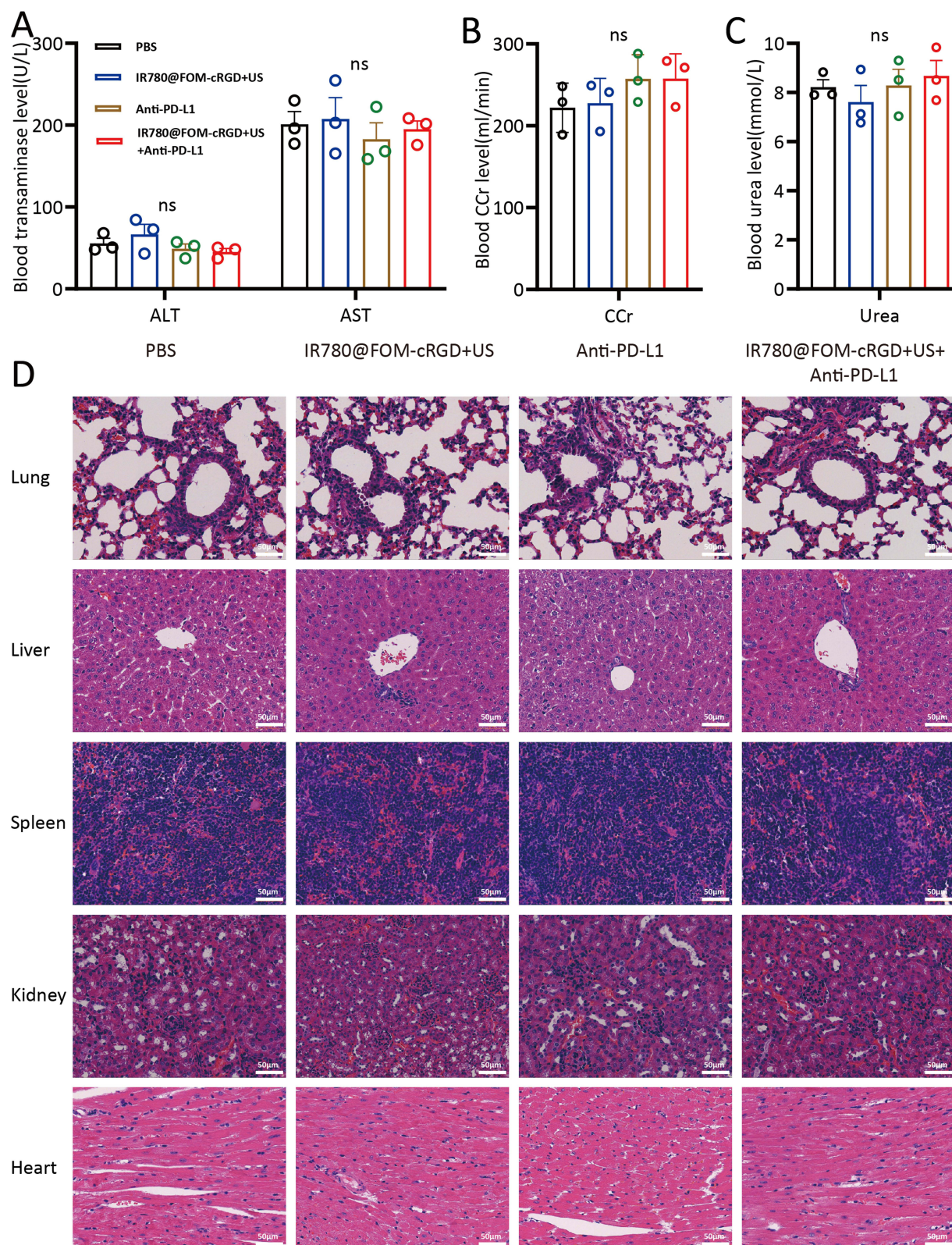


Figure 8 Safety evaluation of Anti-PD-L1 combined with nano-sonodynamic therapy in tumor therapy. **(A–C)** On day 18 after tumor formation, serum was collected from mice in the PBS group, IR780@FOM-cRGD+US group, Anti-PD-L1 group, and IR780@FOM-cRGD+US+Anti-PD-L1 group to measure the levels of ALT and AST **(A)**, CCr **(B)**, and Urea **(C)**. **(D)** The lungs, liver, spleen, kidneys, and heart of each group of mice were also subjected to HE staining analysis to observe changes in cell morphology and assess normal cell damage. Statistical analysis was conducted using a two-tailed non-paired *t*-test, where significance levels were denoted as follows: ns stands for no significant difference.

associated antigens (TAAs) to the tumor site followed by HCC thermal ablation. This approach was shown to promote dendritic cell (DC) maturation and enhance effector T-cell tumor infiltration.⁵⁵ Our findings further demonstrate that effective sonodynamic therapy (SDT) can promote the maturation of dendritic cells (DCs). Immunohistochemical analysis revealed significant increases in the levels of CD3 and CD8 in tumors following treatment with IR780@FOM-cRGD+US+Anti-PD-L1, indicating an enhanced T-cell response (Figure 7C and SIIF-1G). Additionally, the levels of calreticulin (CRT), a marker of immunogenic cell death, were significantly elevated, while the expression of the immunosuppressive protein FoxP3 was markedly reduced post-treatment (Figure 7C and SI1H-1I). These results suggest that the combination of Anti-PD-L1 with nanoscale sonodynamic therapy not only promotes immunogenic cell death but also effectively counteracts immune checkpoint-based suppression, thereby robustly activating the mouse's anti-tumor immune response. This combination of ICD and immune checkpoint blockade (ICB) highlights a potent strategy for enhancing anti-tumor immunity.

Safety Evaluation of Anti-PD-L1 Combined with Nano-Sonodynamic Therapy in Mouse Tumor Treatment

Hepatocellular carcinoma patients often suffer from varying degrees of liver dysfunction due to factors such as liver cirrhosis, which often hinders the application of traditional treatment methods.⁵⁶ The nanomaterials designed in this study are engineered for high targeting specificity. The combination therapy utilizing IR780@FOM-cRGD+US+Anti-PD-L1 is designed to selectively kill tumor cells while activating the body's intrinsic anti-tumor immunity, potentially ensuring a high safety profile. To assess this, liver and kidney function tests were conducted post-treatment, along with hematoxylin and eosin (H&E) staining of various tissue organs. The biosafety analysis revealed no significant alterations in liver and kidney function indicators such as aspartate transaminase (AST), alanine aminotransferase (ALT), endogenous creatinine clearance rate (CCr), and urea in the serum of mice across all treatment groups before and after therapy (Figure 8A-C). Additionally, immunohistochemical staining showed no treatment-related damage to vital organs such as the liver, spleen, kidney, heart, and lungs of the mice (Figure 8D). These findings underscore the safety of combining Anti-PD-L1 with nano-sonodynamic therapy in mouse models of tumor treatment, highlighting its potential suitability for clinical applications.

Conclusions

This study successfully synthesized Fe₃O₄ micelles, specifically IR780@FOM-cRGD, which demonstrated suitable size, particle size distribution, and stability, while exhibiting good biocompatibility in both cellular and mouse models. These nanomicelles effectively targeted tumor cells, releasing high levels of energy and reactive oxygen species (ROS) under ultrasound activation. This activity not only directly killed tumor cells but also inhibited their invasion, migration, and apoptosis. Additionally, the nanomicelles showcased robust near-infrared imaging capabilities, indicating their potential for integrated diagnostic and therapeutic applications.

Importantly, the integration of nanomicelle-based sonodynamic therapy with Anti-PD-L1 treatment combined immunogenic cell death (ICD) and immune checkpoint blockade (ICB), enhancing anti-inflammatory cytokine expression, dendritic cell (DC) maturation, and T cell activation. This comprehensive immune activation led to significant anti-tumor effects, demonstrating the therapeutic potential of this non-invasive strategy for treating deep-seated tumors without significant damage to the liver, kidneys, or other critical organs, affirming its biosafety.

Future studies will aim to enhance the real-time monitoring and prognosis evaluation of these nanomicelles throughout the treatment process. This innovative approach offers a promising strategy for the diagnosis and treatment of liver cancer and presents a viable method for clinical translation.

Ethical Statement

All animal experiments were approved by the Ethics Committee for Animal Welfare of Guangxi Medical University (Ethics number: LW2024064), and were conducted in compliance with the China National Standard GB/T35892-2018 Guidelines for Ethical Review of Laboratory Animal Welfare.

Acknowledgments

This work was supported by grants from the National Natural Science Foundation of China (NSFC) (No. 82360537, 81860502) and the Key Laboratory of Early Prevention and Treatment for Regional High Frequency Tumor, Ministry of Education / Guangxi Key Laboratory of Early Prevention and Treatment for Regional High Frequency Tumor (GKE-ZZ202309, GKE-ZZ202216, GKE-ZZ202129, GKE-ZZ202004). The key project of the Guangxi Science and Technology Department (Gui Ke AB16380242). The research project funded by the Self-raised Funds of the Health Commission of Guangxi Zhuang Autonomous Region (Z20210697). This research was supported by Youth Program of Scientific Research Foundation of Guangxi Medical University Cancer Hospital.

Disclosure

The authors declare that they have no conflicts of interest in this work.

References

1. Sung H, Ferlay J, Siegel RL, et al. Global cancer statistics 2020: GLOBOCAN estimates of incidence and mortality worldwide for 36 cancers in 185 countries. *CA Cancer J Clin*. 2021;71(3):209–249. doi:10.3322/caac.21660
2. de Beijer M, Bezstarosti K, Luijten R, et al. Immunoepitidome of hepatocytes isolated from patients with HBV infection and hepatocellular carcinoma. *JHEP Rep*. 2022;4(11):100576. doi:10.1016/j.jhepr.2022.100576
3. Rodriguez MM, Onorato A, Cantero MJ, et al. 4-methylumbelliferone-mediated polarization of M1 macrophages correlate with decreased hepatocellular carcinoma aggressiveness in mice. *Sci Rep*. 2021;11(1):6310. doi:10.1038/s41598-021-85491-0
4. Liu R, He X, Li Z. Positive clinical outcomes following therapy with programmed cell death protein 1/programmed cell death ligand 1 inhibitors in neuroendocrine carcinoma of the cervix. *Front Pharmacol*. 2022;13:1029598. doi:10.3389/fphar.2022.1029598
5. Antonia SJ, Borghaei H, Ramalingam SS, et al. Four-year survival with nivolumab in patients with previously treated advanced non-small-cell lung cancer: a pooled analysis. *Lancet Oncol*. 2019;20(10):1395–1408. doi:10.1016/S1470-2045(19)30407-3
6. Robert C, Long GV, Brady B, et al. Nivolumab in previously untreated melanoma without BRAF mutation. *N Engl J Med*. 2015;372(4):320–330. doi:10.1056/NEJMoa1412082
7. Finn RS, Qin S, Ikeda M, et al. Atezolizumab plus bevacizumab in unresectable hepatocellular carcinoma. *N Engl J Med*. 2020;382(20):1894–1905. doi:10.1056/NEJMoa1915745
8. Qiu Y, Wu Z, Chen Y, et al. Nano ultrasound contrast agent for synergistic chemo-photothermal therapy and enhanced immunotherapy against liver cancer and metastasis. *Adv Sci (Weinh)*. 2023;10(21):e2300878. doi:10.1002/advs.202300878
9. Nam GH, Lee EJ, Kim YK, et al. Combined Rho-kinase inhibition and immunogenic cell death triggers and propagates immunity against cancer. *Nat Commun*. 2018;9(1):2165. doi:10.1038/s41467-018-04607-9
10. Chen Z, Liu W, Yang Z, et al. Sonodynamic-immunomodulatory nanostimulators activate pyroptosis and remodel tumor microenvironment for enhanced tumor immunotherapy. *Theranostics*. 2023;13(5):1571–1583. doi:10.7150/thno.79945
11. Yin Y, XingwuSun L, HongyanSu C, et al. Continuous inertial cavitation evokes massive ROS for reinforcing sonodynamic therapy and immunogenic cell death against breast carcinoma. *Nano Today*. 2021;36(1):101009. doi:10.1016/j.nantod.2020.101009
12. Um W, Ko H, You DG, et al. Necroptosis-inducible polymeric nanobubbles for enhanced cancer sonoimmunotherapy. *Adv Mater*. 2020;32(16):e1907953. doi:10.1002/adma.201907953
13. Si Y, Yue J, Liu Z, et al. Phase-transformation nanoparticle-mediated sonodynamic therapy: an effective modality to enhance anti-tumor immune response by inducing immunogenic cell death in breast cancer. *Int J Nanomed*. 2021;16:1913–1926. doi:10.2147/IJN.S297933
14. Xu L, Zhang W, Park HB, et al. Indocyanine green and poly I:C containing thermo-responsive liposomes used in immune-photothermal therapy prevent cancer growth and metastasis. *J Immunother Cancer*. 2019;7(1):220. doi:10.1186/s40425-019-0702-1
15. Liu Y, Pagacz J, Wolfgeher DJ, Bromerg KD, Gorman JV, Kron SJ. Senescent cancer cell vaccines induce cytotoxic T cell responses targeting primary tumors and disseminated tumor cells. *J Immunother Cancer*. 2023;11(2):e005862. doi:10.1136/jitc-2022-005862
16. Li H, Liu Z, Han C. Clinical value of prophylactic transcatheter arterial chemoembolization treatment in patients with hepatocellular carcinoma. *Am J Transl Res*. 2022;14(5):3225–3232.
17. Nguyen Cao TG, Kang JH, Kim W, et al. Engineered extracellular vesicle-based sonotheranostics for dual stimuli-sensitive drug release and photoacoustic imaging-guided chemo-sonodynamic cancer therapy. *Theranostics*. 2022;12(3):1247–1266. doi:10.7150/thno.65516
18. Feng Y, Wang H, Zhang S, et al. Antibodies@MOFs: an in vitro protective coating for preparation and storage of biopharmaceuticals. *Adv Mater*. 2019;31(2):e1805148. doi:10.1002/adma.201805148
19. Wang W, Xu X, Li Z, Lendlein A, Ma N. Genetic engineering of mesenchymal stem cells by non-viral gene delivery. *Clin Hemorheol Microcirc*. 2014;58(1):19–48. doi:10.3233/CH-141883
20. Gaharwar US, Meena R, Rajamani P. Biodistribution, clearance and morphological alterations of intravenously administered iron oxide nanoparticles in male wistar rats. *Int J Nanomed*. 2019;14:9677–9692. doi:10.2147/IJN.S223142
21. Ulbrich K, Holá K, Šubr V, Bakandritsos A, Tuček J, Zbořil R. Targeted drug delivery with polymers and magnetic nanoparticles: covalent and noncovalent approaches, release control, and clinical studies. *Chem Rev*. 2016;116(9):5338–5431.
22. Zhang X, Ng H, Lu A, et al. Drug delivery system targeting advanced hepatocellular carcinoma: current and future. *Nanomedicine*. 2016;12(4):853–869. doi:10.1016/j.nano.2015.12.381
23. Wang Z, Wu P, He Z, et al. Mesoporous silica nanoparticles with lactose-mediated targeting effect to deliver platinum(IV) prodrug for liver cancer therapy. *J Mater Chem B*. 2017;5(36):7591–7597. doi:10.1039/C7TB01704A

24. Bao YW, Hua XW, Chen X, Wu FG. Platinum-doped carbon nanoparticles inhibit cancer cell migration under mild laser irradiation: multi-organelle-targeted photothermal therapy. *Biomaterials*. 2018;183:30–42.
25. Xu ZZ, Xiu P, Lv JW, et al. Integrin $\alpha\beta 3$ is required for cathepsin B-induced hepatocellular carcinoma progression. *Mol Med Rep*. 2015;11(5):3499–3504. doi:10.3892/mmr.2014.3140
26. Zhang PF, Li KS, Shen YH, et al. Galectin-1 induces hepatocellular carcinoma EMT and sorafenib resistance by activating FAK/PI3K/AKT signaling. *Cell Death Dis*. 2016;7(4):e2201. doi:10.1038/cddis.2015.324
27. Li S, Wei J, Yuan L, et al. RGD-modified endostatin peptide 30 derived from endostatin suppresses invasion and migration of HepG2 cells through the $\alpha\beta 3$ pathway. *Cancer Biother Radiopharm*. 2011;26(5):529–538. doi:10.1089/cbr.2011.0978
28. Bi-Yuan Z, Xiao-Qing Y, Yang Z, et al. Synthesis and photodynamic activities of integrin-targeting silicon(IV) phthalocyanine-cRGD conjugates. *Eur J Med Chem*. 2018;155:24–33. doi:10.1016/j.ejmech.2018.05.039
29. Hsu CY, Wang PW, Alalawi A, Lin ZC, Fang JY. Use of lipid nanocarriers to improve oral delivery of vitamins. *Nutrients*. 2019;11(1):68. doi:10.3390/nu11010068
30. Qureshi KA, Mohammed S, Khan O, Ali HM, El-Readi MZ, Mohammed HA. Cinnamaldehyde-based self-nanoemulsion (CA-SNEDDS) accelerates wound healing and exerts antimicrobial, antioxidant, and anti-inflammatory effects in rats' skin burn model. *Molecules*. 2022;27(16):5225. doi:10.3390/molecules27165225
31. Song J, Ye H, Jiang S, Yang Y, Li X. An acid response IR780-based targeted nanoparticle for intraoperative near-infrared fluorescence imaging of ovarian cancer. *Int J Nanomed*. 2022;17:4961–4974. doi:10.2147/IJN.S375145
32. Chen S, Wang J, Liao H, et al. M1 macrophage-derived sonoresponsive nanoparticles for sonodynamic anticancer therapy. *Int J Nanomed*. 2022;17:4725–4741. doi:10.2147/IJN.S381170
33. Razumova S, Brago A, Barakat H, et al. Evaluation of the microbiological effect of colloidal nanosilver solution for root canal treatment. *J Funct Biomater*. 2022;13(4):163. doi:10.3390/jfb13040163
34. Adachi SI, Kondo S, Sato Y, Yoshizawa F, Yagasaki K. Anti-hyperuricemic effect of isorhamnetin in cultured hepatocytes and model mice: structure-activity relationships of methylquercetin as inhibitors of uric acid production. *Cytotechnology*. 2019;71(1):181–192. doi:10.1007/s10616-018-0275-8
35. Zhou Y, Sun X, Zhou L, Zhang X. pH-sensitive and long-circulation nanoparticles for near-infrared fluorescence imaging-monitored and chemo-photothermal synergistic treatment against gastric cancer. *Front Pharmacol*. 2020;11:610883. doi:10.3389/fphar.2020.610883
36. Shen FF, Chen Y, Dai X, et al. Purely organic light-harvesting phosphorescence energy transfer by β -cyclodextrin pseudorotaxane for mitochondria targeted imaging. *Chem Sci*. 2020;12(5):1851–1857. doi:10.1039/D0SC05343K
37. Yin Y, Hu B, Yuan X, Cai L, Gao H, Yang Q. Nanogel: a versatile nano-delivery system for biomedical applications. *Pharmaceutics*. 2020;12(3):290. doi:10.3390/pharmaceutics12030290
38. Huang J, Liu F, Han X, et al. Nanosonosensitizers for highly efficient sonodynamic cancer theranostics. *Theranostics*. 2018;8(22):6178–6194. doi:10.7150/thno.29569
39. Huang B, Wang L, Tang K, et al. IR780 based sonotherapeutic nanoparticles to combat multidrug-resistant bacterial infections. *Front Chem*. 2022;10:840598. doi:10.3389/fchem.2022.840598
40. Hu Z, Song X, Ding L, et al. Engineering Fe/Mn-doped zinc oxide nanosonosensitizers for ultrasound-activated and multiple ferroptosis-augmented nanodynamic tumor suppression. *Mater Today Bio*. 2022;16:100452. doi:10.1016/j.mtbio.2022.100452
41. An J, Hu YG, Cheng K, et al. ROS-augmented and tumor-microenvironment responsive biodegradable nanopatform for enhancing chemo-sonodynamic therapy. *Biomaterials*. 2020;234:119761. doi:10.1016/j.biomaterials.2020.119761
42. Cheng Y, Cheng H, Jiang C, et al. Perfluorocarbon nanoparticles enhance reactive oxygen levels and tumour growth inhibition in photodynamic therapy. *Nat Commun*. 2015;6:8785. doi:10.1038/ncomms9785
43. Li Y, Wang Y, Gao L, et al. Betulinic acid self-assembled nanoparticles for effective treatment of glioblastoma. *J Nanobiotechnology*. 2022;20(1):39. doi:10.1186/s12951-022-01238-7
44. Kaibori M, Kosaka H, Matsui K, et al. Near-infrared fluorescence imaging and photodynamic therapy for liver tumors. *Front Oncol*. 2021;11:638327. doi:10.3389/fonc.2021.638327
45. Domińska M, Pastuch-Gawolek G, Skonieczna M, Szeja W, Domiński A, Kurcok P. Glycoconjugation of quinoline derivatives using the C-6 position in sugars as a strategy for improving the selectivity and cytotoxicity of functionalized compounds. *Molecules*. 2022;27(20):6918. doi:10.3390/molecules27206918
46. Kroemer G, Galluzzi L, Kepp O, Zitvogel L. Immunogenic cell death in cancer therapy. *Annu Rev Immunol*. 2013;31:51–72. doi:10.1146/annurev-immunol-032712-100008
47. Ghebeh H, Mohammed S, Al-Omair A, et al. The B7-H1 (PD-L1) T lymphocyte-inhibitory molecule is expressed in breast cancer patients with infiltrating ductal carcinoma: correlation with important high-risk prognostic factors. *Neoplasia*. 2006;8(3):190–198. doi:10.1593/neo.05733
48. Wu C, Zhu Y, Jiang J, Zhao J, Zhang XG, Xu N. Immunohistochemical localization of programmed death-1 ligand-1 (PD-L1) in gastric carcinoma and its clinical significance. *Acta Histochem*. 2006;108(1):19–24. doi:10.1016/j.acthis.2006.01.003
49. Zitvogel L, Apetoh L, Ghiringhelli F, Kroemer G. Immunological aspects of cancer chemotherapy. *Nat Rev Immunol*. 2008;8(1):59–73. doi:10.1038/nri2216
50. Chang K, Qu Y, Dai B, et al. PD-L1 expression in Xp11.2 translocation renal cell carcinoma: indicator of tumor aggressiveness. *Sci Rep*. 2017;7(1):2074. doi:10.1038/s41598-017-02005-7
51. Chen D, Wu X, Xie C. Nivolumab for metastatic urothelial cancer in a renal allograft recipient with subsequent graft rejection and treatment complete remission: a case report. *Front Oncol*. 2021;11:646322. doi:10.3389/fonc.2021.646322
52. Aoki T, Kudo M, Ueshima K, et al. Exploratory analysis of lenvatinib therapy in patients with unresectable hepatocellular carcinoma who have failed prior PD-1/PD-L1 checkpoint blockade. *Cancers*. 2020;12(10):3048. doi:10.3390/cancers12103048
53. Lebedeva A, Fitzgerald W, Molodtsov I, Shpektor A, Vasileva E, Margolis L. Differential clusterization of soluble and extracellular vesicle-associated cytokines in myocardial infarction. *Sci Rep*. 2020;10(1):21114. doi:10.1038/s41598-020-78004-y
54. Obeid M, Panaretakis T, Tesniere A, et al. Leveraging the immune system during chemotherapy: moving calreticulin to the cell surface converts apoptotic death from "silent" to immunogenic. *Cancer Res*. 2007;67(17):7941–7944. doi:10.1158/0008-5472.CAN-07-1622

55. Xiao Z, Li T, Zheng X, et al. Nanodrug enhances post-ablation immunotherapy of hepatocellular carcinoma via promoting dendritic cell maturation and antigen presentation. *Bioact Mater.* 2023;21:57–68. doi:10.1016/j.bioactmat.2022.07.027
56. Di Sebastiano P, Festa L, Büchler MW, Di Mola FF. Surgical aspects in management of hepato-pancreatico-biliary tumours in the elderly. *Best Pract Res Clin Gastroenterol.* 2009;23(6):919–923. doi:10.1016/j.bpg.2009.10.003

International Journal of Nanomedicine

Dovepress

Publish your work in this journal

The International Journal of Nanomedicine is an international, peer-reviewed journal focusing on the application of nanotechnology in diagnostics, therapeutics, and drug delivery systems throughout the biomedical field. This journal is indexed on PubMed Central, MedLine, CAS, SciSearch®, Current Contents®/Clinical Medicine, Journal Citation Reports/Science Edition, EMBase, Scopus and the Elsevier Bibliographic databases. The manuscript management system is completely online and includes a very quick and fair peer-review system, which is all easy to use. Visit <http://www.dovepress.com/testimonials.php> to read real quotes from published authors.

Submit your manuscript here: <https://www.dovepress.com/international-journal-of-nanomedicine-journal>